RSC Advances

PAPER

View Article Online
View Journal | View Issue

Cite this: *RSC Adv.*, 2015, **5**, 33392

Ultralong mesoporous ZnO nanowires grown *via* room temperature self-assembly of ZnO nanoparticles for enhanced reversible storage in lithium ion batteries†

Hong-Jie Yang, Suh-Ciuan Lim, Sheng-Yan He and Hsing-Yu Tuan*

Received 24th January 2015
Accepted 31st March 2015

DOI: 10.1039/c5ra01423a

www.rsc.org/advances

A facile template-free method for the synthesis of high purity ultralong mesoporous ZnO nanowires (up to 50 μm) has been developed. ZnO nanoparticles were first formed by decomposition of the $Zn(Ac)_2$–OLA complex in supercritical hexane at 430 °C for 20 min. Afterward, porous ZnO nanowires were produced though *in situ* self-aggregation of ZnO nanoparticles at room temperature under the cooperation of oleylamine and porous metal–organic frameworks which coordinate ZnO nanoparticles aggregated together in the form of 1D porous nanostructures. Due to the porous structures, the obtained porous ZnO nanowires have a larger surface area than those of ZnO nanoparticles and ZnO nanowires which have solid structures. Furthermore, compared to the poor capacity performance of ZnO powders, giving a capacity of only around 120 mA h g^{-1} at 10th cycles at 0.1 C charge/discharge rate, the porous ZnO nanowire electrode shows a reversible capacity of 432 mA h g^{-1} after 50 cycles. The improved capacity and cycle life of the porous ZnO nanowires electrode was attributed to the structure which gives rise to more efficient Li ion transport and alleviates the large mechanical strain during lithiation and delithiation.

Introduction

One dimensional (1D) nanostructures (length > 1 μm) such as nanobelts, nanowires, and nanotubes have received great attention due to their promising physical properties and potential applications in developing novel electronic, opto-electronic, and thermoelectric nanodevices.[1–9] To synthesize 1D nanostructures, introducing driving forces to promote or inhibit the growth rate of specific directions during the crystal growth period is needed. Until now, a variety of strategies have been developed for the growth of 1D nanostructures, including the vapor–liquid–solid (VLS) mechanism, alumina membrane-confined growth, screw dislocation driven growth, and seed mediated growth.[10–16] Among these methods, the VLS growth is the most widely used method to synthesize nanowires through intentional use of metal nanoparticles during the crystal growth period in the gas phase and this concept has been applied to the solution phase (solution–liquid–solid, SLS and supercritical fluid–liquid–solid, SFLS) in the past few decades.[17–19] In addition to the classical crystal growth model (atom addition) for the growth of 1D nanostructures (above-mentioned), another type for the growth of 1D nanostructures is the nanoparticle based aggregation model (oriented attachment) which uses existing nanocrystals as building blocks to build single crystalline 1D or complex-shaped nanostructures.[20]

Zinc oxide (ZnO) is an inexpensive and environmental friendly semiconductor materials with n-type direct band gap and large excitation binding energy (60 meV) for promising optical and piezoelectric properties.[21–24] ZnO can exist in the forms of a diverse group of nanomaterials such as nanorods, nanowires, nanobelts, nanotubes, and nanorings because of the wurtzite structures and polar surface.[25] Compared to the solid structures of nanomaterials, porous structures have received a lot of attention due to their promising characteristics such as large surface area, high surface to-volume ratio, and facile mass transport in materials, which are potentially useful in the fields of catalysis, hydrogen storage, sensors, separation, and secondary batteries.[26–29] For example, porous ZnO nanostructures grown on a copper foil as anode materials of lithium ion batteries exhibit better cycle performance and rate capabilities than those of commercial ZnO powders.[28] Nowadays, only few studies have successfully synthesized porous 1D ZnO nanomaterials which are generally produced based on template methods such as porous anodic alumina membrane and pre-preparation of 1D nanostructures template (ZnSe or zinc salt) combined annealing processes for preparing porous ZnO nanowires.[29–35]

In this article, a new approach to synthesize ultralong mesoporous ZnO nanowires with high purity is reported. The

Department of Chemical Engineering, National Tsing Hua University, 101, Section 2, Kuang-Fu Road, Hsinchu, Taiwan 30013. E-mail: hytuan@che.nthu.edu.tw; Fax: +886-3-571-5408; Tel: +886-3-572-3661

† Electronic supplementary information (ESI) available: XRD and UV-vis absorption spectra of ZnO nanowires obtained from different time periods. See DOI: 10.1039/c5ra01423a

growth is based on self-aggregation of ZnO nanoparticles at room temperature. Under room temperature self-assembled period, the ZnO nanoparticles can fuse together in the form of 1D direction and accompany with extending their length (up to 50 μm) with increasing self-assembled time. Comparing to the template methods, our approach provides a simple, template free, and catalyst-free way to synthesize ultralong porous ZnO nanowires. In addition, the possible growth mechanism of the porous ZnO nanowires was monitored and explained by SEM, FTIR, and NMR techniques. Firstly, small ZnO nanoparticles were produced though thermal decomposition of Zn acetate–oleylamine complex under supercritical hexane at 430 °C and then these small ZnO nanoparticles self aggregated, *in situ*, onto porous nanowires with the assistance of porous metal–organic frameworks and oleylamine at room temperature. The unique optical properties and the Brunauer–Emmett–Teller (BET) surface area of the porous ZnO nanowires are also measured. Finally, the electrochemical properties of porous ZnO nanowires as LIBs anodes are presented.

Experimental section

Chemicals

Zinc acetate ($Zn(Ac)_2$, 99.99%), oleylamine (OLA, 70%), anhydrous hexane (95%) were purchased from Aldrich. 1 M $LiPF_6$ in 1 : 1 (v/v) ethylene carbonate/dimethyl carbonate (electrolyte), Celgard membrane (separator), Li metal foil (99.9%), Cu metal foil (0.01 mm), polyvinylidene fluoride (PVDF), *N*-methyl-2-pyrrolidone (NMP, 99%), Super-P carbon black, and coin-type half-cells (CR2032) were purchased from SYNergy ScienTech Corp.

Synthesis of ultralong ZnO nanowires

To prepare the Zn stock solution, $Zn(Ac)_2$ (24 mmol) was added to OLA (24 mmol) in a 20 mL glass sample vial. The mixture was degassed with Ar and stirred at 100 °C for 24 h, the color of solution was changed to yellow and became very viscous indicating that $Zn(Ac)_2$–OLA complex was formed, the Zn stock solution was stored in a nitrogen-filled glove box for further used.

Supercritical fluid reaction was carried out in a 10 mL stainless steel reactor and connected to a high-pressure (1/16″ i.d.) tubing *via* a LM-6 HIP (High Pressure Equipment Co.) reducer. The tubing was connected to a six-way valve (Valco) with a 0.5 mL injection loop. The reactor was covered with heating tape and the temperature was controlled by a temperature controller. A high pressure liquid chromatography (HPLC) pump was used to pressurize the reactor system and the pressure was monitored with a digital pressure gauge.

In a typical porous ZnO nanowires synthesis, the gas in the reactor was replaced with nitrogen, then the reactor was heated to 430 °C and pressurized to 500 psi by injecting hexane. The reactant solution (Zn stock solution without dilution) was brought out from the glove box and injected into a 0.5 mL injection loop. Next, the HPLC pump was turned on at a 2 mL min^{-1} injection rate to pressurize the reactor system. When the system pressure reached 2000 psi, the injection flow was turned off and the inlet valve was closed. The reaction was maintained at 430 °C for 20 min. Afterward, the reactor was immersed in a water bath and maintained at this stage for more than 6 hour to obtain ultralong ZnO nanowires. All of the ZnO nanostructures were collected for further characterization.

Characterization

Scanning electron microscopy (SEM) images were recorded using either a SEM, Hitachi S-2300 or a HITACHI-S4700 FESEM, operating at 10 kV or 15 kV accelerating voltage. For transmission electron microscopy (TEM) sample preparation, ZnO nanostructures dispersed in hexane were drop-casted onto 200-mesh carbon-coated copper grids. TEM was performed using a JEOL JEM-3000F operating at 300 kV equipped with an Oxford INCA energy-dispersive X-ray spectrometer. X-ray diffraction (XRD) was prepared by drying a ZnO nanostructures solution on Si substrates. The XRD patterns were recorded on a Rigaku, Ultima IV X-ray diffractometer using Cu Kα radiation ($\lambda = 0.15418$ nm). UV-vis absorption and photoluminescence (PL) samples were performed by measuring dispersion of porous ZnO nanowires in hexane. UV-vis absorption and PL spectra were obtained using a Hitachi U-4100 spectrophotometer and a Hitachi F-4500 fluorescence spectrophotometer, respectively. FTIR spectra were recorded with KBr using a Perkin-Elmer Spectrum RXI FTIR spectrometer in the range of 4000–600 cm^{-1} with 32 scans. The ^1H NMR spectrums were recorded on a Varian UnityInova 500 NMR spectrometer using TMS as an internal reference at 25 °C. The N_2 adsorption–desorption isotherms were estimated at 77 K using NOVA e1000, Quantachrome. Surface areas and pore size distribution were determined by the Brunauer–Emmett–Teller (BET) method and the Barrett–Joyner–Halenda (BJH) method, respectively.

Electrochemical characterization

The composite electrode was prepared by mixing active materials (40 wt%) with 40 wt% of Super-P carbon black and 20 wt% of PVDF binder in NMP solvent to form a homogeneous slurry, which was then spread onto a copper foil. The coin-type half-cells (CR2032) were assembled in an Ar-filled glove box and prepared out of a composite electrode as the working electrode, Li metal foil as the counter electrode, and Celgard membrane soaked in electrolyte. Cycle capacity of the free standing NW fabric was evaluated using a Maccor Series 4000 Battery Test System instrument. The electrode capacity was calculated based on the weight of the active materials and the weight of pure active material was measured using a microbalance with 0.1 μg resolution (Sartorius SE2).

Results and discussions

Fig. 1 shows the SEM images of the product obtained after thermal decomposition of $Zn(Ac)_2$–OLA complex followed by a water bath process, indicating that the products have a wire shape with honeycomb-like patterns. Fig. 1c and d are the close-up view of the honeycomb-like patterns, revealing that the patterns are indeed composed of nanowires with diameters

ranging from 90 to 180 nm and lengths over 50 μm. The honeycomb-like patterns may be caused by surface tension effects (capillary forces) of the evaporating hexane between the nanowires, just like previous reports.[36,37] Fig. 2c shows a XRD pattern of the nanowires. The pattern exhibits well-resolved peaks characteristic and all reflection peaks can be indexed as wurtzite ZnO [space group $P6_3mc$, JCPDS Card no. 36-1451] with lattice constants $a = 3.25$ Å and $c = 5.21$ Å. The room temperature optical absorption and PL spectra of the as-synthesized ZnO nanowires are also measured (Fig. 2a and b). The absorption maximum is about 366 nm. The PL spectra shows two emission bands, one strong and narrow band is centered at 379 nm (3.27 eV) attributed to the near band edge emission; another weak and broad emission band ranging between 430 and 560 nm is assigned to the deep level emission due to surface defects in the ZnO nanowires.[38–40]

More structural information of as-synthesized nanowires was examined with TEM images, selected area electron diffraction (SAED) and, energy-dispersive X-ray spectroscopy (EDS) patterns. The porous structure inside nanowires can be shown more clearly in TEM images (Fig. 3a and b), where the light and dark parts correspond to the pores and the ZnO nanoparticles, indicating the random and well-defined porous structures in the nanowires. A SAED pattern of individual ZnO nanowire with a diameter of about 100 nm (Fig. 3b) is shown in Fig. 3c suggesting a polycrystalline structure and the disordered aggregation of the ZnO nanocrystals. All diffraction rings on the SAED pattern could be indexed respectively to (100), (002), (101), (102), (110), (103), and (200) lattice planes of wurtzite crystal structure of ZnO, which is the same crystal structure observed in the XRD measurement. EDS recorded from a single porous nanowire is given in Fig. 3d, showing Zn, O, and Cu elements, suggesting that the composition of the porous nanowire is ZnO (Cu signal in the spectrum is from the Cu grid). Moreover, scanning transmission electron microscope-energy-dispersive X-ray spectroscopy (STEM-EDS) mapping was also recorded to demonstrate the homogeneous distribution of Zn and O elements in the porous nanowires (Fig. 3e–g).

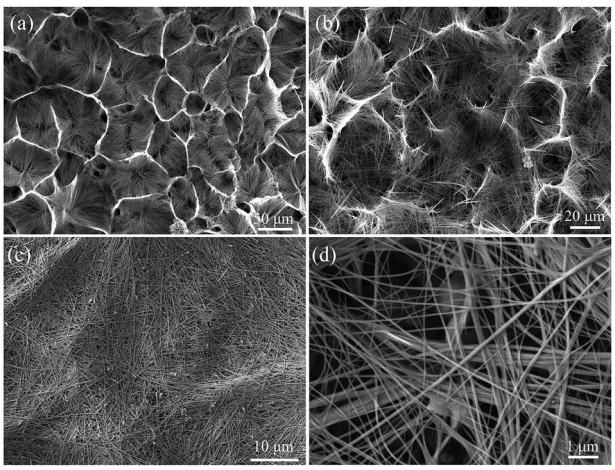

Fig. 1 (a–d) SEM images of the ultralong porous ZnO nanowires. The products were fabricated by thermal decomposition of $Zn(Ac)_2$–OLA complex under supercritical hexane at 430 °C for 20 min followed by water bath process for 24 h.

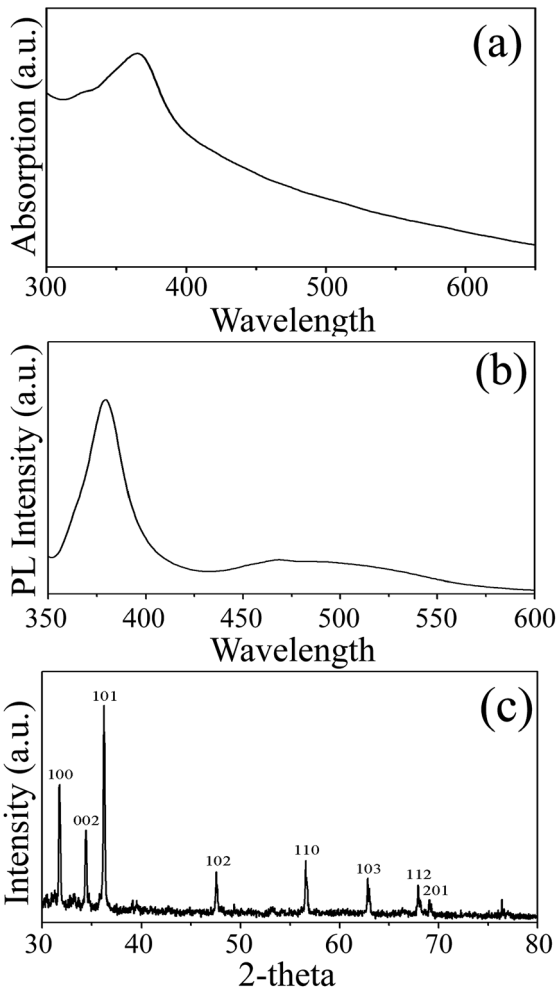

Fig. 2 (a) UV-vis absorption, (b) PL spectra, and (c) XRD pattern of porous ZnO nanowires.

Further detailed structural information of porous ZnO nanowires is provided by the HRTEM images. Fig. 4a–d show TEM images of four individual ZnO porous nanowires and Fig. 4e–h show their corresponding HRTEM images, respectively. These HRTEM images show that the ZnO porous nanowires having clear contrast difference are composed of disordered aggregation of nanoparticles with distinct lattice fringe patterns, which confirms the polycrystalline and porous character of the ZnO nanowires. Compared with single crystalline nanowires having smooth surface, the porous ZnO nanowires possess rough surface because they are constructed by random aggregation of ZnO nanoparticles. In addition, HRTEM images present the lattice fringes of nanocrytallites with a spacing of 0.26 nm and 0.24 nm, which corresponds to the (002) planes and (101) lattice planes of the wurtzite crystal structure of ZnO, respectively. The size distribution and average size of these nanoparticles estimated from HRTEM images are around 2.5–5.1 nm and 3.8 nm, respectively. According to TEM, HRTEM, SAED, and EDS analysis, the ZnO nanowires having porous structure are constructed by random aggregation of

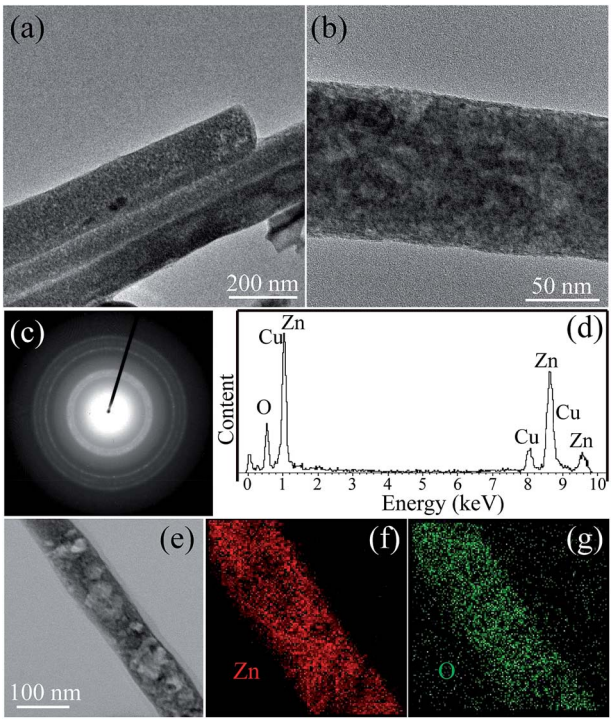

Fig. 3 (a and b) TEM images, (c) SAED pattern, and (d) EDS spectra of porous ZnO nanowires. (e–g) STEM-EDS mapping profile of Zn (red) and O (green) in the porous ZnO nanowires.

small ZnO nanoparticles with main size range of 2.5–5.1 nm and average size of 3.8 nm. The discrepancy of average size between TEM statistics and XRD calculation might due to the agglomeration of the small nanoparticles, some defects in the crystallites and the difference between TEM and XRD techniques for measuring the particle size.[32] The aggregation of these nanoparticles leads to the formation of the porous structure of ZnO nanowires, thus resulting in more surface area in BET analysis (see discussion below).

The measurement of N_2 adsorption–desorption isotherms of the porous nanostructures had been performed. Fig. 5 displays the N_2 adsorption–desorption isotherm and the pore size distribution of the porous ZnO nanowires (inset). The characteristic feature of the curves can be identified as the type IV, indicating the mesoporous materials. The mesoporosity was further verified by the pore size distribution curve as shown in the inset of Fig. 5 The analysis shows one narrow peak centered at about 3.1 nm and most of the pores sizes are located between 3 and 7 nm, indicating that the material has a narrower pore size distribution with an average pore diameter around 14.5 nm. The surface area for the porous ZnO nanowires is 50 $m^2\ g^{-1}$ based on the BET model and the pore volume was 0.14 $cm^3\ g^{-1}$. The surface area of the porous ZnO nanowires is significantly greater than that of commercial ZnO powder (surface area of 10 $m^2\ g^{-1}$ to 16 $m^2\ g^{-1}$).[41] We propose that the pores are attributed to the interparticle space generating from the self aggregation of the individual ZnO nanoparticles. However, the obtained surface areas are not very high, probably

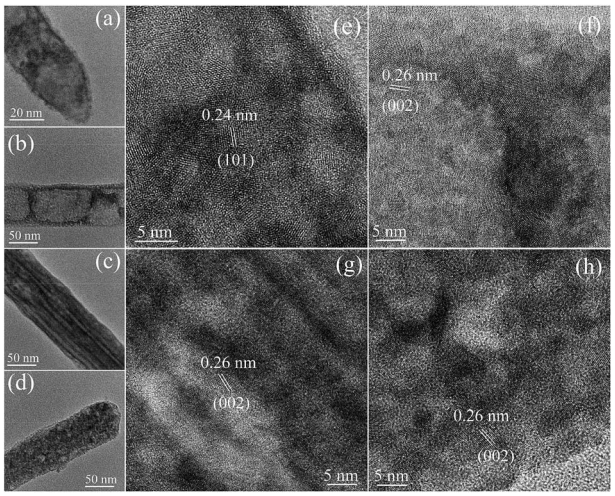

Fig. 4 (a–d) TEM images of four individual ZnO porous nanowires and their corresponding (e–h) HRTEM images.

due to some pores were block by the random aggregated nanoparticles.

In order to observe the growth process and morphological evolution of the porous ZnO nanowires, SEM images of the products at different time intervals from the reaction have been performed. Fig. 6 shows SEM images of the ZnO nanostructures obtained at reaction time of 0 min, 20 min, 3 h, and 4 h in the water bath process. The UV-vis absorption spectra and XRD patterns of ZnO nanostructures obtained at reaction time of 0 min, 20 min, 3 h were shown in ESI (Fig. S1 and S2†). We can know that the products are mainly composed of nanoparticles (Fig. 6a) just after the high temperature process (heating at 430 °C for 20 min). After 20 min of water bath process, bundle shape products (minority products) with some nanoparticles began to appear and the bundle shaped products are constructed by about 2 μm long nanowires (Fig. 6b). As the reaction time of water bath process was continuously increased, the shape of the bundle products changed to honeycomb-like patterns probably because the length of the nanowires increase significantly and the capillary forces between

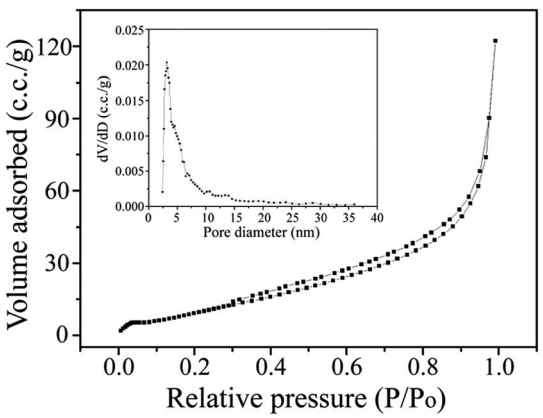

Fig. 5 N_2 adsorption–desorption isotherms and (inset) pore size distribution of the porous ZnO nanowires.

nanowires during drying (Fig. 6c and d), the length of the nanowires increases from 2 μm (20 min) to 8 μm (4 h). As the reaction time of water bath process continuously proceed (24 h), the diameter of the porous nanowires shows no significant change, but the length of the nanowires continuously increases to over 50 μm in length (Fig. 1).

To better understand and explain the possible growth mechanism of the porous ZnO nanowire, FTIR and NMR have also been performed. Fig. 7 shows the FTIR spectra of OLA, $Zn(Ac)_2$, $Zn(Ac)_2$–OLA complex, residual liquid after high temperature process (430 °C, 20 min), and residual liquid after water bath process for 5 h. Pure OLA with symmetric and asymmetric alkane CH_2 stretches and symmetric rocking mode of terminal methyl group at ~2850 cm^{-1}, ~2931 cm^{-1}, and ~1466 cm^{-1} can be detected. In addition, NH_2 scissoring region is visible at 1622 cm^{-1}.[42] For $Zn(Ac)_2$, the 696 cm^{-1} band is attributed to zinc acetate, the 622 cm^{-1} band is contributed by a Zn–O stretching vibration, and the bands at 1552 and 1456 cm^{-1} are typical for the asymmetric and symmetric C=O stretching in acetate groups.[43] When $Zn(Ac)_2$–OLA complex was formed, those characteristic peaks that were observed in pure OLA and $Zn(Ac)_2$ can be still measured and the bands assigned to asymmetric and symmetric C=O stretching in acetate groups become wider. In addition, according to the ^1H NMR spectra (Fig. 8), the bands with chemical shift at ~1.1 ppm will shift to 4.1 ppm after $Zn(Ac)_2$ and OLA heated to 100 °C for 24 h. Accordance with previous report, the degree of the drift is relative to the degree of amine protonation.[44] These results support that the $Zn(Ac)_2$–OLA complex was formed. After high temperature process, a new peak at with chemical shift at ~5.8 ppm in the ^1H NMR spectra (Fig. 8) is appeared, indicating *N*-oleyl acetamide will generate after high temperature process, consistent with previous reports.[45] Furthermore, we also know that residual liquid still contains OLA, $Zn(Ac)_2$, and $Zn(Ac)_2$–OLA complex from FTIR and ^1H NMR spectra, indicating that the precursor solution is not completely decomposed.

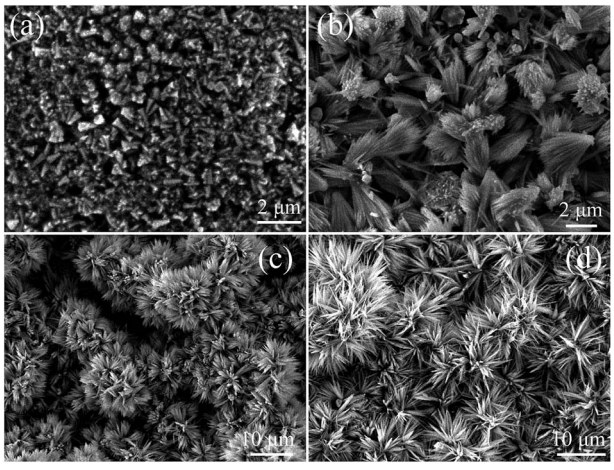

Fig. 6 SEM images of the ZnO nanostructures obtained after high temperature process at different reaction time intervals in the water bath process: (a) 0 min, (b) 20 min, (c) 3 h, and (d) 4 h.

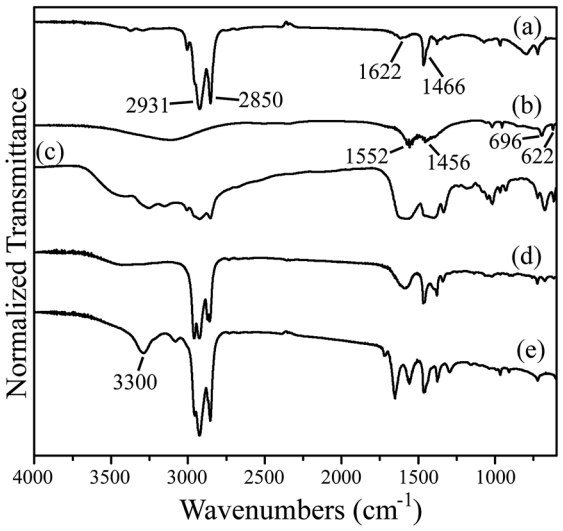

Fig. 7 FTIR spectra of (a) OLA, (b) $Zn(Ac)_2$, (c) $Zn(Ac)_2$–OLA complex, (d) residual liquid just after high temperature process (430 °C, 20 min), and (e) residual liquid after water bath process for 5 h.

According to the above results, we understand that the OLA, $Zn(Ac)_2$, and $Zn(Ac)_2$–OLA complex will remain in the reactor system after high temperature process. We speculate that the residual OLA, $Zn(Ac)_2$, and $Zn(Ac)_2$–OLA complex are the main forces for the formation of porous ZnO nanowires. Firstly, previous reports indicate that the $Zn(Ac)_2$ decomposing under inert atmosphere might form porous metal–organic frameworks with the multi-dentate groups.[43,46] Two large bands for the asymmetric and symmetric C=O stretching in acetate groups become wider after $Zn(Ac)_2$–OLA complex formed from FTIR spectra might be several overlapping peaks attributing to a variety of forms of acetate complexes (three possible structures for the $Zn(Ac)_2$ complex, unidentate, bidentate, and bridging), and a band from the bidentate carbonate groups at about 3300 cm^{-1} appears after water bath for 5 h.[47,48] It supports the reactor system might exist metal–organic frameworks with the multi-dentate groups. Therefore, when the reaction is continuously proceed in the stage of water bath, the porous metal–organic frameworks might be bound to the existing ZnO nanostructure surface or between the ZnO nanostructure surface leaving a void and help the porous structure formed. Secondly, it is well known that the organic ligand has a great influence on the final shape of nanomaterials. In our system, we assume that the OLA also plays a key role in the formation of porous ZnO nanowires. Fig. 9 shows the schematic diagram of the formation of porous ZnO nanowires. From the observation of SEM images that many ZnO nanoparticles will generated just after high temperature process due to the high concentration and high injection flow rate of precursors. As the reaction proceeds, these ZnO nanoparticles self-aggregated to form porous ZnO nanowires with the help of OLA for lowering the system energy, just like previous case.[35,49] In addition, OLA is not only aiding aggregation of nanoparticles into 1D nanowires but also acting like capping ligand to prevent further growth of ZnO nanoparticles. As a result, the porous ZnO nanowires was

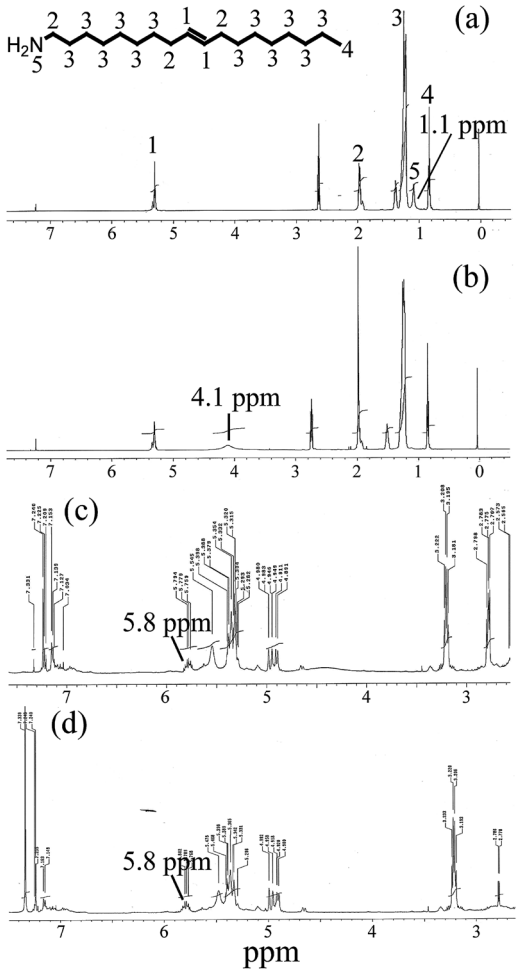

Fig. 8 ^{1}H NMR spectra of (a) OLA, (b) $Zn(Ac)_2$–OLA complex, (c) residual liquid just after high temperature process (430 °C, 20 min), and (d) residual liquid after water bath process for 5 h recorded in $CDCl_3$ at 500 MHz and 25 °C.

formed by the cooperation of porous metal–organic frameworks that may provide a void foster the formation of porous structure and OLA that aid the self-aggregation of ZnO nanoparticles, but we must state that the exact growth mechanism is still needed further investigation.

The electrochemical performance of the porous ZnO nanowires was also investigated. Fig. 10a shows the voltage profiles of the porous ZnO nanowires electrode, all plateaus in the voltage profiles during charge and discharge are consistent with the differential capacity plots. The first charge and discharge capacities of porous ZnO nanowires electrode are 1392 mA h g^{-1} and 728 mA h g^{-1} giving an initial Coulombic efficiency of 52.3%. The voltage profile and differential capacity results are shown in Fig. 10b. In the first scan, two cathodic peaks at about 0.15 V and 0.5 V during lithiation reactions can be assigned to the formation of lithium–zinc alloy and the reduction of ZnO into Zn, respectively. Upon delithiation, three anodic peaks in the potential range of 0–0.8 V correspond to the delithiation of lithium–zinc alloy. The relatively large initial irreversible capacity loss of the porous ZnO nanowires electrode was

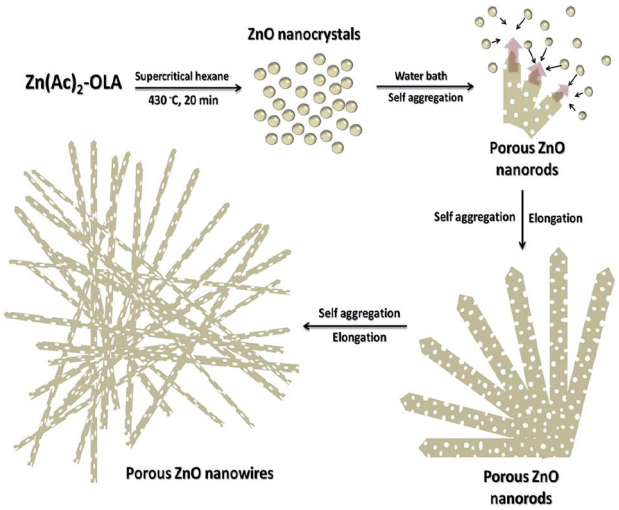

Fig. 9 Schematic diagram of the formation of porous ZnO nanowires by self-aggregated mechanism.

attributed to the formation of more solid electrolyte interface (SEI) layer or irreversible lithium insertion into the host materials because of large surface area compared to the commercial ZnO powders. It is possible that the capacity loss related to multiple nanocracks that causes larger volume expansion at one side and bending of nanowires during the first cycle of lithium insertion and extraction.[50] Previous studies on lithiation of similar material such as silicon cause self-expansion of embedded nanoparticles component that disrupted electron conductivity of nanocomposites and generated a new SEI layer to reduce the rechargeable capacity.[51] Moreover, some degree of irreversibility was also observed by a previous case of intercalation of Li ions in amorphous TiO_2 nanotubes.[52] Fig. 10c shows galvanostatic cycling results of porous ZnO nanowires and commercial ZnO powders at 0.1 C rate. For commercial ZnO powders, the first charge and discharge capacities are 676 mA h g^{-1} and 457 mA h g^{-1}, respectively, which corresponds to a Coulombic efficiency of 67.6%. The capacities of commercial ZnO powders electrode rapidly degrade to 120 mA h g^{-1} within several cycles and the porous ZnO nanowires electrode exhibits charge and discharge capacities of 432 and 420 mA h g^{-1}, respectively, at the 50th cycle. Fig. 10d shows the rate capability of the porous ZnO nanowires at various current densities, including 0.2 C, 0.5 C, 1 C and 2 C in the voltage range of 0.01–3.0 V. The initial discharge capacities of 758, 444, 338, and 269 mA h g^{-1} were obtained at 0.2, 0.5, 1, and 2 C, respectively. The capacity recovered to ~480 mA h g^{-1} at 0.2 C after a cycle of 20 times with different charge/discharge densities. While integrated in a supercapacitor electrode with proper aspect ratio, ZnO nanowires exhibited excellent ability to transport electrolytes effectively and shorten ion diffusion path.[53] In similar case, ZnO–CoO/PCM porous nanocomposite was demonstrated for a lithium ion battery anode, resulting better cycling stability than a non-porous ZnO–CoO/carbon black mixture.[54] The improved capacity and cycle life of the porous ZnO nanowires electrode can be attributed to the porous structure which provides more reaction area for Li transport to alleviate large mechanical strain

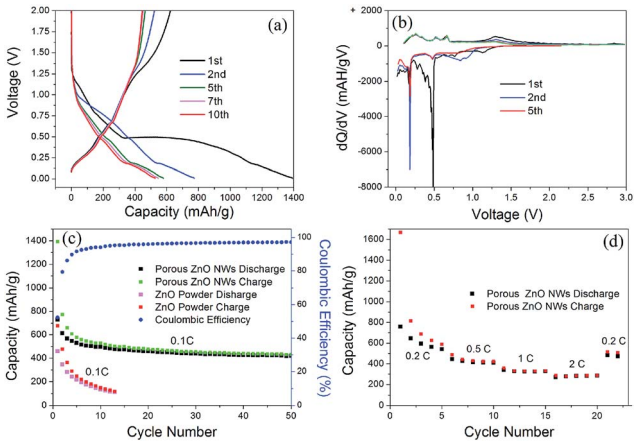

Fig. 10 (a) Galvanostatic charge–discharge curves and (b) differential capacity curves of porous ZnO nanowires electrode. (c) Cycling performance of porous ZnO nanowires and ZnO powders electrodes. (d) Comparison of the rate capability at various current densities: 0.2 C, 0.5 C, 1 C and 2 C.

during the process of lithiation and delithiation. Moreover, the porous structure can also limit the particle volume expansion at full lithiation and prevent pulverization in bulk particles, which is similar to previous case of porous silicon.[55]

Conclusions

In summary, we have successful synthesized ultralong (>50 μm) porous ZnO nanowires composed by random aggregation of small ZnO nanoparticles. Compared with the commonly used template synthesis, our approach is a simple way to produce large quantity of porous ZnO nanowires. We propose a possible growth mechanism of the porous ZnO nanowires based on SEM, FTIR, and NMR analysis results. Firstly, small ZnO nanoparticles would generate due to the high precursor concentration with high injection rate in the high temperature process. Afterward, these small ZnO nanoparticles start to self aggregate to form porous ZnO nanowires under the assistance of porous metal–organic frameworks and OLA at room temperature. This nanoparticle-based aggregation growth to build porous ZnO nanowires is different from the well known particle based crystallization, and oriented attachment mechanism. 1D nanostructure growth *via* an oriented attachment mechanism typically has solid structure and single crystal characteristics because oriented attachment mechanism is a particle based crystallization process.[56] In our approach, we think that the porous ZnO nanowires are constructed by random aggregation of small ZnO nanoparticle and there is no apparent particle based crystallization appears in the aggregation process, resulting in polycrystalline nature and porous structures in the ZnO nanowires. We believe that the porous metal–organic frameworks and OLA are the directing agent for the formation of porous ZnO nanowires, similar to the previous reports.[49] In addition, the surface area and pore size distribution of the porous ZnO nanowire are 50 m^2 g^{-1} and mainly between 3 and 7 nm. The electrochemical properties of porous ZnO nanowires as LIBs anodes show improved capacity and cycle life compared to the ZnO powder electrodes due to higher surface area of the porous ZnO nanowire for effecting Li ion transport and better toleration of mechanical strain than those of ZnO nanoparticles and ZnO nanowires with solid structure.

Acknowledgements

The authors acknowledge the financial support by the Ministry of Science and Technology of Taiwan (NSC 102-2221-E-007-023-MY3, MOST 103-2221-E-007-089-MY3, and NSC 101-2623-E-007-013-IT), the Ministry of Economic Affairs, Taiwan (101-EC-17-A-09-S1-198), National Tsing Hua University (102N2051E1), and the assistance from Center for Energy and Environmental Research, National Tsing-Hua University.

Notes and references

1 T. Zhai, L. Li, Y. Ma, M. Liao, X. Wang, X. Fang, J. Yao, Y. Bandoa and D. Golberg, *Chem. Soc. Rev.*, 2011, **40**, 2986–3004.
2 B. Su, Y. Wu and L. Jiang, *Chem. Soc. Rev.*, 2012, **41**, 7832–7856.
3 F.-Y. Yuan, H.-J. Yang and H.-Y. Tuan, *J. Mater. Chem.*, 2011, **21**, 13793–13800.
4 S. Xu and Z. L. Wang, *Nano Res.*, 2011, **4**, 1013–1098.
5 X. Wen, W. Wu, Y. Ding and Z. L. Wang, *J. Mater. Chem.*, 2012, **22**, 9469–9476.
6 C. X. Guo, S. Huang and X. Lu, *Green Chem.*, 2014, **16**, 2571–2579.
7 V. Malgras, P. Jood, Z. Sun, S. X. Dou, Y. Yamauchi and J. H. Kim, *Chem.–Eur. J.*, 2014, **20**, 10451–10455.
8 Y. Li, B. P. Bastakoti, M. Imura, S. M. Hwang, Z. Sun, J. H. Kim, S. X. Dou and Y. Yamauchi, *Chem.–Eur. J.*, 2014, **20**, 6027–6032.
9 C. Li, M. Imura and Y. Yamauchi, *Chem.–Eur. J.*, 2014, **20**, 3277–3282.
10 Y. Wu, R. Fan and P. Yang, *Nano Lett.*, 2002, **2**, 83–86.
11 N. I. Kovtyukhova and T. E. Mallouk, *Nanoscale*, 2011, **3**, 1541–1552.
12 F. Meng, S. A. Morin, A. Forticaux and S. Jin, *Acc. Chem. Res.*, 2013, **46**, 1616–1626.
13 H.-J. Yang, S.-Y. He and H.-Y. Tuan, *Langmuir*, 2014, **30**, 602–610.
14 Y. Yamauchi, *J. Ceram. Soc. Jpn.*, 2013, **1417**, 831–840.
15 N. Suzuki, T. Kimurab and Y. Yamauchi, *J. Mater. Chem.*, 2010, **20**, 5294–5300.
16 Y. Yamauchi, N. Suzukia and T. Kimura, *Chem. Commun.*, 2009, 5689–5691.
17 X. Lu, D. D. Fanfair, K. P. Johnston and B. A. Korgel, *J. Am. Chem. Soc.*, 2005, **127**, 15718–15719.
18 H.-Y. Tuan and B. A. Korgel, *Chem. Mater.*, 2008, **20**, 1239–1241.
19 J. D. Holmes, D. M. Lyons and K. J. Ziegler, *Chem.–Eur. J.*, 2003, **9**, 2144–2150.
20 Q. Zhang, S.-J. Liu and S.-H. Yu, *J. Mater. Chem.*, 2009, **19**, 191–207.

21 M. H. Huang, S. Mao, H. Feick, H. Q. Yan, Y. Y. Wu, H. Kind, E. Weber, R. Russo and P. D. Yang, *Science*, 2001, **292**, 1897–1899.
22 X. Y. Kong and Z. L. Wang, *Nano Lett.*, 2003, **3**, 1625–1631.
23 Z. W. Pan, Z. R. Dai and Z. L. Wang, *Science*, 2001, **291**, 1947–1949.
24 P. Zu, Z. K. Tang, G. K. L. Wong, M. Kawasaki, A. Ohtomo, H. Koinuma and Y. Segawa, *Solid State Commun.*, 1997, **103**, 459–463.
25 B. Weintraub, Z. Zhou, Y. Li and Y. Deng, *Nanoscale*, 2010, **2**, 1573–1587.
26 M. Ahmad, Rafi-ud-Din, C. F. Pan and J. Zhu, *J. Phys. Chem. C*, 2010, **114**, 2560–2565.
27 A. Hagfeldt, G. Boschloo, L. C. Sun, L. Kloo and H. Pettersson, *Chem. Rev.*, 2010, **110**, 6595–6663.
28 X. H. Huang, X. H. Xia, Y. F. Yuan and F. Zhou, *Electrochim. Acta*, 2011, **56**, 4960–4965.
29 H. Q. Wang, G. H. Li, L. C. Jia, G. Z. Wang and C. J. Tang, *J. Phys. Chem. C*, 2008, **112**, 11738–11743.
30 Z. Gui, J. Liu, Z. Z. Wang, L. Song, H. Yuan, W. C. Fan and D. Y. Chen, *J. Phys. Chem. B*, 2005, **109**, 1113–1117.
31 Z. D. Hu, Q. Chen, Z. Li, Y. Yu and L. M. Peng, *J. Phys. Chem. C*, 2010, **114**, 881–889.
32 C. X. Shan, Z. Liu, Z. Z. Zhang, D. Z. Shen and S. K. Hark, *J. Phys. Chem. B*, 2006, **110**, 11176–11179.
33 R. Q. Song, A. W. Xu, B. Deng, Q. Li and G. Y. Chen, *Adv. Funct. Mater.*, 2007, **17**, 296–306.
34 Y. H. Xiao, L. Li, Y. Li, M. Fang and L. D. Zhang, *Nanotechnology*, 2005, **16**, 671–674.
35 F. Ye, Y. Peng, G. Y. Chen, B. Deng and A. W. Xu, *J. Phys. Chem. C*, 2009, **113**, 10407–10415.
36 K. K. S. Lau, J. Bico, K. B. K. Teo, M. Chhowalla, G. A. J. Amaratunga, W. I. Milne, G. H. McKinley and K. K. Gleason, *Nano Lett.*, 2003, **3**, 1701–1705.
37 C. H. Lu, L. M. Qi, J. H. Yang, L. Tang, D. Y. Zhang and J. M. Ma, *Chem. Commun.*, 2006, 3551–3553.
38 Y. S. Fu, X. W. Du, S. A. Kulinich, J. S. Qiu, W. J. Qin, R. Li, J. Sun and J. Liu, *J. Am. Chem. Soc.*, 2007, **129**, 16029–16033.
39 K. Matsuyama, K. Mishima, T. Kato, K. Irie and K. Mishima, *J. Colloid Interface Sci.*, 2012, **367**, 171–177.
40 X. S. Tang, E. S. G. Choo, L. Li, J. Ding and J. M. Xue, *Chem. Mater.*, 2010, **22**, 3383–3388.
41 N. Daneshvar, S. Aber, M. S. S. Dorraji, A. R. Khataee and M. H. Rasoulifard, *Sep. Purif. Technol.*, 2007, **58**, 91–98.
42 H.-J. Yang, S.-Y. He, H.-L. Chen and H.-Y. Tuan, *Chem. Mater.*, 2014, **26**, 1785–1793.
43 S. Bhattacharyya and A. Gedanken, *Microporous Mesoporous Mater.*, 2008, **110**, 553–559.
44 J. W. Thomson, K. Nagashima, P. M. Macdonald and G. A. Ozin, *J. Am. Chem. Soc.*, 2011, **133**, 5036–5041.
45 Z. H. Zhang, M. H. Lu, H. R. Xu and W. S. Chin, *Chem.–Eur. J.*, 2007, **13**, 632–638.
46 M. Eddaoudi, H. L. Li and O. M. Yaghi, *J. Am. Chem. Soc.*, 2000, **122**, 1391–1397.
47 G. B. Deacon and R. J. Phillips, *Coord. Chem. Rev.*, 1980, **33**, 227–250.
48 S. Sakohara, M. Ishida and M. A. Anderson, *J. Phys. Chem. B*, 1998, **102**, 10169–10175.
49 X. Cao, N. Wang, L. Wang and L. Guo, *J. Nanopart. Res.*, 2010, **12**, 143–150.
50 A. Kushima, X. H. Liu, G. Zhu, Z. L. Wang, J. Y. Huang and J. Li, *Nano Lett.*, 2011, **11**, 4535–4541.
51 M. Gu, Y. Li, X. L. Li, S. Y. Hu, X. W. Zhang, W. Xu, S. Thevuthasan, D. R. Baer, J. G. Zhang, J. Liu and C. M. Wang, *ACS Nano*, 2012, **6**, 8439–8447.
52 Q. Gao, M. Gu, A. M. Nie, F. Mashayek, C. M. Wang, G. M. Odegard and R. Shahbazian-Yassar, *Chem. Mater.*, 2014, **26**, 1660–1669.
53 Q. Yang, X. T. Zhang, M. Y. Zhang, Y. Gao, H. Gao, X. C. Liu, H. Liu, K. W. Wong and W. M. Lau, *J. Power Sources*, 2014, **272**, 654–660.
54 L. J. Liu, C. Y. Zhao, H. L. Zhao, Q. Y. Zhang and Y. Li, *Electrochim. Acta*, 2014, **135**, 224–231.
55 X. L. Li, M. Gu, S. Y. Hu, R. Kennard, P. F. Yan, X. L. Chen, C. M. Wang, M. J. Sailor, J. G. Zhang and J. Liu, *Nat. Commun.*, 2014, **5**, 4105.
56 C. Pacholski, A. Kornowski and H. Weller, *Angew. Chem., Int. Ed.*, 2002, **41**, 1188–1191.